

Effect of Tool Geometry and Heat Input on the Hardness, Grain Structure, and Crystallographic Texture of Thick-Section Friction Stir-Welded Aluminium



M.M.Z. AHMED, B.P. WYNNE, W.M. RAINFORTH, ADRIAN ADDISON, J.P. MARTIN, and P.L. THREADGILL

The effect of tool geometries on the microstructure and crystallographic texture of 32-mm-thick friction stir-welded AA6082 has been investigated. The use of a tapered probe tool results in a significant variation in the grain size from the top to the base of the nugget, whereas parallel probe tools produce a uniform grain size throughout the nugget. The grain size in the nugget reflects the amount of deformation experienced and the speed of deformation expressed in terms of strain rate. An approach is proposed to calculate the strain rate during FSW of aluminum for which values between 217 and 362 s⁻¹ were obtained. The strain rate can be either uniform or varied through the joint thickness based on the type of tool used. The tapered tool produces a variation of the strain rate, whilst the parallel tool has a uniform strain rate throughout, which can explain the obtained grain structure in each case. The tool geometries also influenced texture development with the tapered tool producing a tilt of the local shear reference frame by an angle to the normal direction equal to the taper angle.

<https://doi.org/10.1007/s11661-018-4996-2>

© The Minerals, Metals & Materials Society and ASM International 2018

I. INTRODUCTION

FRICITION stir welding (FSW)^[1] is a well-established solid state joining process for a variety of metals and alloys and is used in a wide range of applications.^[2–5] The FSW tool plays a major role in the solid state joining process, including 1. heating the abutted plates in order to soften the surrounding material and 2. moving the softened material from the front of the tool to the back of the tool in order to develop the joint.^[6–24] The effect of the tool geometry on weld microstructure and crystallographic texture has not been explored in detail, especially for thick-section aluminum.

A few studies have been carried out to examine the effect of tool geometry on microstructure, bonding quality and mechanical properties.^[12,15–17] Boz and Kurt^[17] studied the effect of tool geometry on the bonding and mechanical properties of FS-welded 5-mm-thick AA1080. They examined five different tools, four of them were screw type with a different pitch width of 0.85, 1.10, 1.40, and 2.0 mm pitch and one was a bar with 5 mm × 5 mm square cross section. They obtained best bonding using 0.85 and 1.10 mm pitched tools. They also obtained bonding with the square cross section tool but it had poor mechanical properties. Fujii *et al.*^[16] studied the effect of the tool geometry on the mechanical properties and microstructure of 5-mm thick FSWed 1050-H24, 5083-O, and AA6061-T6. Three different tool geometries were used: a columnar probe without threads, a columnar probe with threads, and a triangular prism probe. They reported that for 1050-H24, a columnar tool without threads produced a weld with the best mechanical properties, whereas for 6061-T6, the tool shape did not significantly affect the microstructures or mechanical properties of the joints. For 5083-O, the weldability was significantly affected by the rotation speed. At a high rotation speed (1500 rpm), the triangular prism tool was the best; at the middle rotation speed (800 rpm), the column with threads was the best, whilst for the low rotation speed (600 rpm), the tool shape did not significantly affect the

M.M.Z. AHMED is with the Mechanical Engineering Department, The British University in Egypt, Al-Sherouk, Cairo 11837, Egypt, with the Department of Materials Science and Engineering, The University of Sheffield, Mappin Street, Sheffield S1 3JD, UK, and also with the Department of Metallurgical and Materials Engineering, Suez University, Suez 43721, Egypt. Contact e-mail: mohamed.zaky@bue.edu.eg B.P. WYNNE and W.M. RAINFORTH are with the Department of Materials Science and Engineering, The University of Sheffield. ADRIAN ADDISON and P.L. THREADGILL are with TWI Ltd, Granta Park, Great Abington, Cambridge CB21 6AL, UK J.P. MARTIN is with TWI Technology Centre Ltd, Wallis Way, Catcliffe, Rotherham, S60 5TZ, UK

Manuscript submitted April 19, 2018.

Article published online November 5, 2018

microstructures or mechanical properties of the joints. Scialpi *et al.*,^[12] on the other hand, studied the effect of tool shoulder geometry on the microstructure and mechanical properties of AA6082 of 1.5 mm thickness. They examined three different shoulders: with filet and scroll; with filet and cavity; and with filet only. They reported that the best joint is formed by a shoulder with filet and cavity. Elangovan and Balasubramanian^[15] studied the effect of the probe profile and rotational speed on the formation of friction stir processing (FSP) zone in AA2219 of 6 mm thickness. They used five different probe profiles of straight cylindrical, threaded cylindrical, tapered cylindrical, square, and triangle tool probe to produce butt welds at different rotation speeds of 1500, 1600, and 1700 rpm at constant travel speed of 46 mm/min. They reported that the square pin-profiled tool produced defect-free FSP region, irrespective of rotational speeds, the joints produced at a rotational speed of 1600 rpm showed better tensile properties, irrespective of tool pin profiles. Also the joint produced using square pin-profiled tool at a rotational speed of 1600 rpm showed superior tensile properties. From the above review it can be said that the effect of the tool geometry on the crystallographic texture of thick-section friction stir welds has not been explored before. Hence this work will focus mainly on the effect of the tool probe geometry on the development of grain structure and crystallographic texture of thick-section friction stir-welded AA6082.

II. EXPERIMENTAL WORK

Three FSW tools of different geometries, shown in Figure 1, have been used to produce five different FS welds with plunge depth of 32 mm in an AA6082-T6 of 38 mm thickness. The first tool called tapered probe tool (TPT) has a shoulder diameter of 40 and 19 mm diameter at the top of the probe and a taper of 28.8 deg to give an extreme difference between the peripheral velocity at the probe tip and probe top. Three flats and a thread-like groove feature were also added to the outer surface of the probe. The second tool used was a parallel probe tool (PPT) of constant 19 mm diameter probe from the top to the bottom again with a shoulder diameter of 40 mm. Three flutes with a ‘slippery’ profile

and a thread-like groove feature were also added. Some care was taken to ensure commonality of as many features as possible between the two probes.

Two thermocouples were also added to the above-mentioned tools, one 5 mm from the tip and one 5 mm below the probe and shoulder junction, Figure 2. Both were placed approximately 5 mm from the outer surface of the tool. It is worthy of note that all the welds were produced using a cold plate underneath, which may have affected the heat dissipation at the bottom of the welds. Each tool was mounted in the spindle of TWI’s ESAB SuperStir™ machine. The thermocouples were connected to the thermal management system and the system calibrated. A gas flame was applied to the tool probe to check the operation of the system. Care was taken to place the tips of the thermocouples at a uniform distance from the outer profile of the probe, to eliminate the effect of thermal conductivity on the temperature reading attained.

The third tool incorporating all the major features of the PPT but with a shoulder diameter of 30 mm and a top probe diameter of 12 mm compared to the original 19 mm was also investigated. Importantly, due to the lower stress regime expected, the tool was manufactured from H13 tool steel, not the more expensive and difficult to source MP159 alloy used for the other tools in this study and for tools of this general size.

Table I shows all trial conditions undertaken. For the TPT and PPT two weld conditions (different traverse and rotation speeds) were used to generate different levels of heat input.

The welds were then sectioned normal to the weld direction (WD) and polished and etched with Keller’s reagent to reveal the microstructure. Vickers hardness was measured with 5 kg load in a two-dimensional grid with a 4-mm spacing in order to construct a hardness map, which could then be correlated with microstructure observations. Detailed Electron Back Scattered Diffraction (EBSD) analysis was then carried out at different positions inside the weld nugget (NG). These samples were cut from the weld cross section in order for them to fit in the microscope. The specimens were mechanically polished and subsequently electropolished with a solution of 30 pct Nitric acid in methanol for 60 seconds at 14 V and – 15 °C. After electropolishing, the samples were then mechanically polished again very

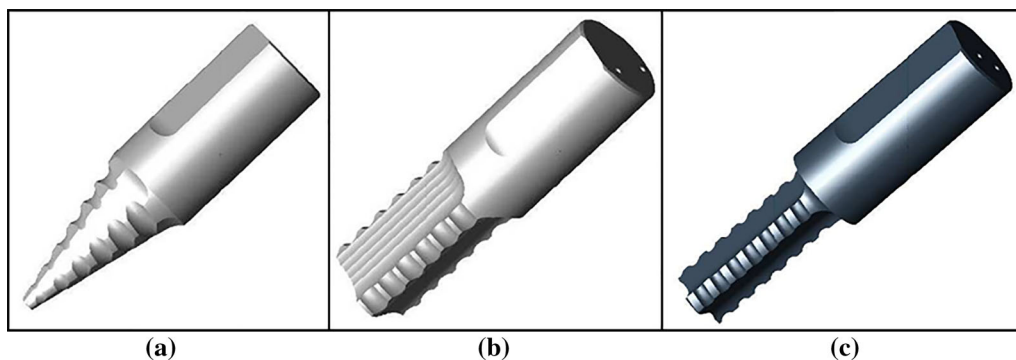


Fig. 1—The three different tools used in this study (a) tapered probe tool (TPT), (b) parallel probe tool (PPT) of 19 mm diameter, and (c) parallel probe tool (PPT) of 12 mm diameter.

gently for very short time just to remove the second phase particles coming up from the surface, which causes a shadowing effect during EBSD acquisition. A Sirion scanning electron microscope equipped with a Nordlys CCD camera controlled by HKL Channel 5 software was used for EBSD data acquisition. For microstructure analysis, a 0.3- μm step size was used and for texture analysis, a 4- μm step size was used. The obtained data were then analyzed using HKL Channel 5 software.

III. RESULTS AND DISCUSSION

A. Optical Macrographs and Hardness

Figure 3 shows optical macrographs of all the welds. All NG profiles follows the tool probe profile, having a

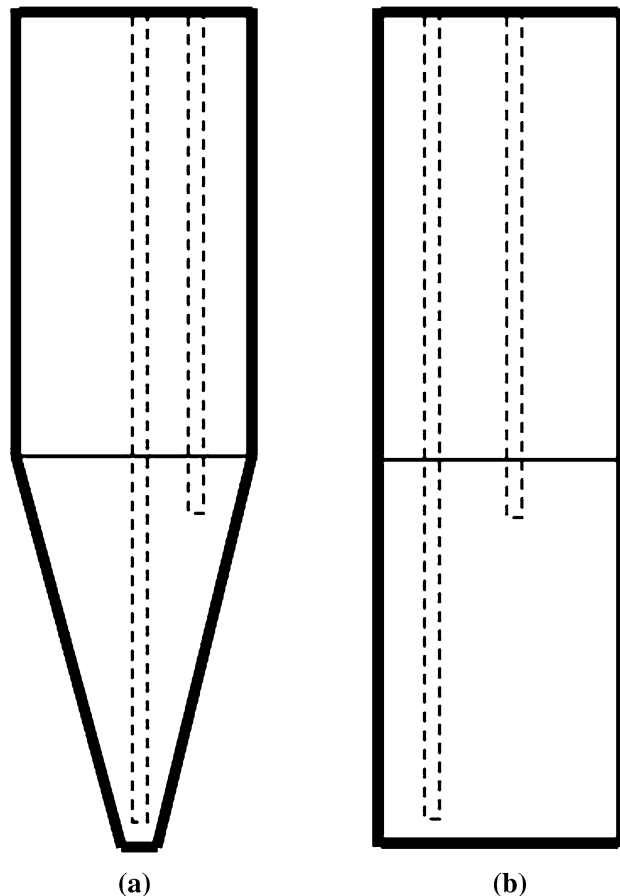


Fig. 2—Schematic of the TPT (a) and PPT (b) showing the thermocouple positions.

triangular profile in the TPT welds and a rectangular profile in the PPT welds. Typical FSW microstructure features such as onion rings (banding structure) and the

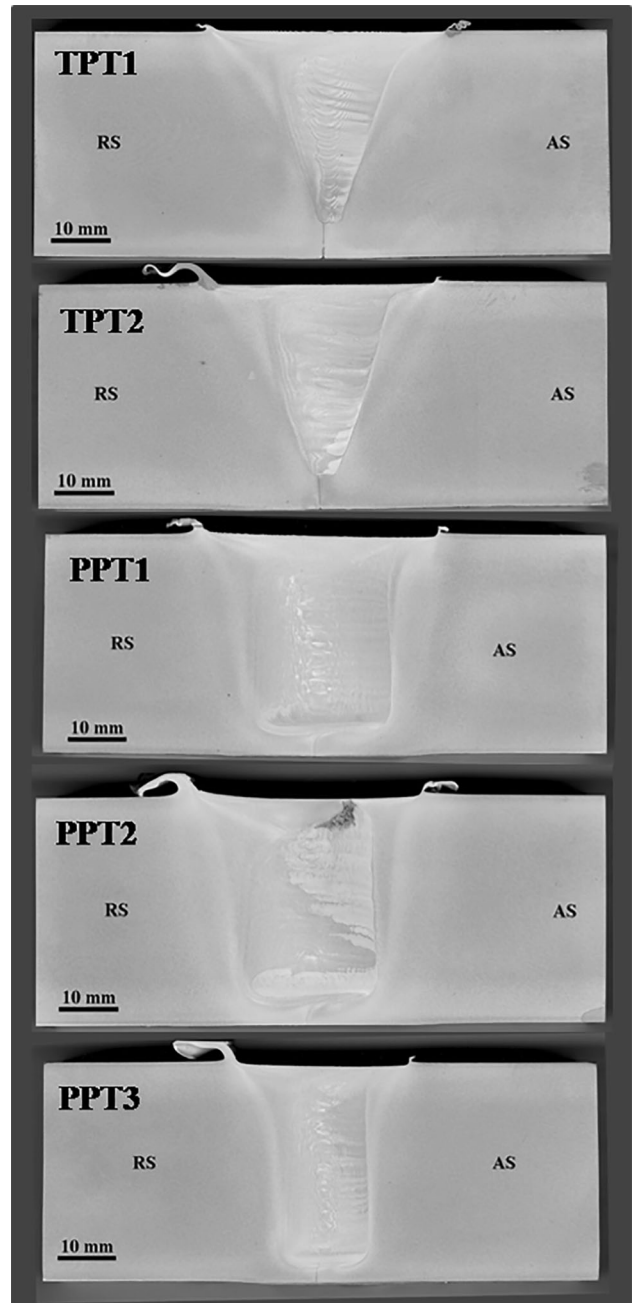


Fig. 3—Optical macrograph of the different 32-mm welds. Each weld name indicated on its macrograph. AS: stands for advancing side and RS: stands for retreating side.

Table I. Friction Stir Welding Parameter Used to Produce the Different Joints

Weld ID.	Rotation Rate (rev/min)	Traverse Speed (mm/min)	Traverse Speed/Rotation Rate (mm/rev)
TPT1	400	125	0.3125
TPT2	500	62.5	0.125
PPT1	400	125	0.3125
PPT2	500	62.5	0.125
PPT3	600	125	0.208

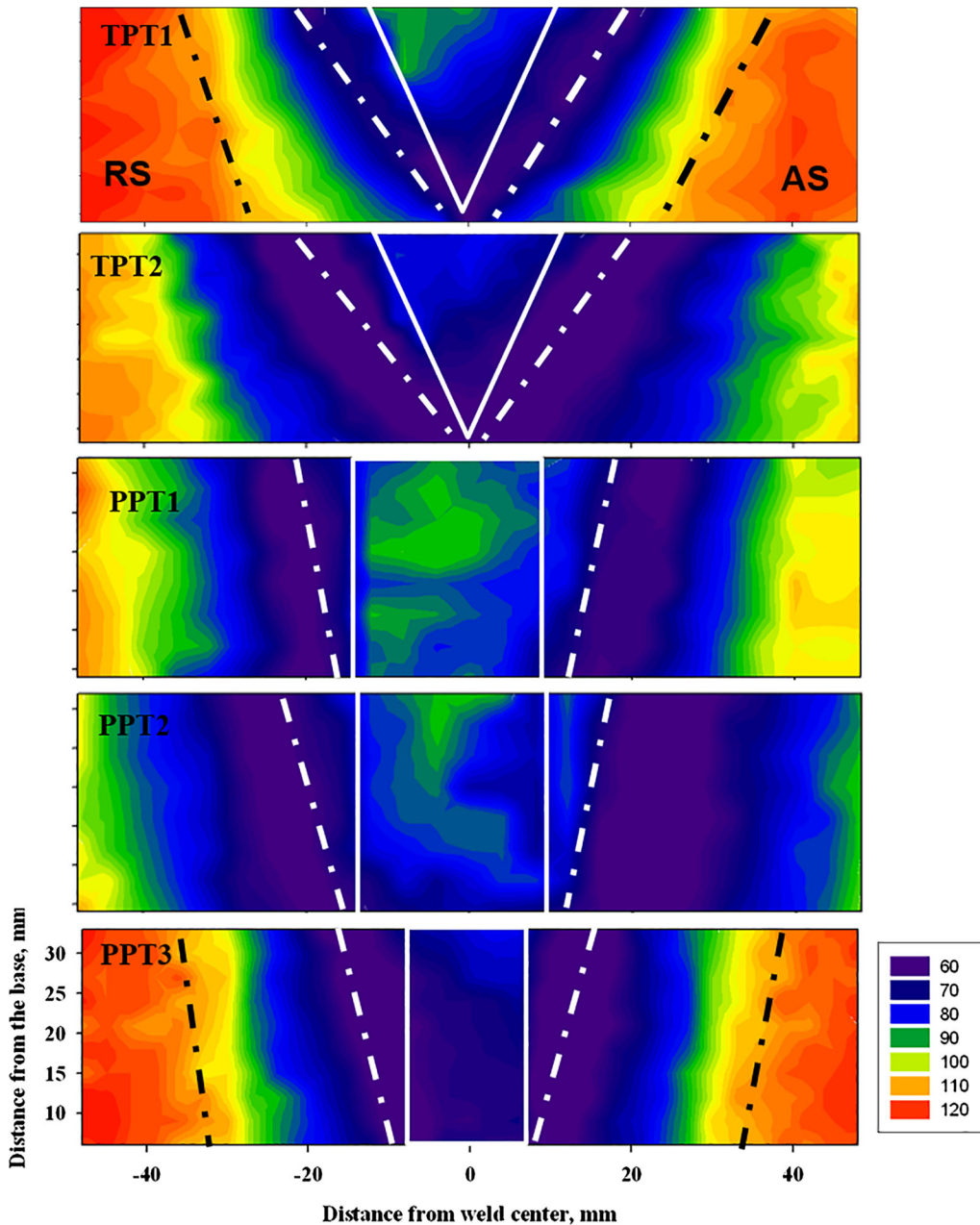


Fig. 4—Vickers hardness maps of the different tool geometries and different heat inputs FS welds. The solid white lines indicate the NG boundaries, dashed white lines indicate the TMAZ boundaries, and dashed black lines indicate the HAZ boundaries.

joint line remnant can be seen clearly in the high-speed welds (TPT1 and PPT1) but are less intense in the low-speed welds (TPT2 and PPT2). Two other features that can only be seen in the PPT2 weld are an unconsolidated region at the top right of the NG and bright regions, which can be seen on the advancing side (AS) of the NG as well as in the bottom of the NG. It should be mentioned here that the ratio between the depth of the probe and the width of the shoulder is above 0.8, which resulted in defect-free joints and that the flat features added to the probe were beneficial to achieve sound joints with a narrow heat-affected zone. This is in good agreement with the work carried out by

Huang *et al.*^[25] to investigate the effect of a high depth-to-width ratio of the tool in the thick-section FSW.

The Vickers hardness distribution across the welds transverse section is presented in Figure 4 with the red color being the highest hardness (~ 120 Hv) and the dark blue being the lowest hardness (~ 60 Hv). In all cases, the hardness decreases from the base material through the heat-affected zone (HAZ), with the lowest hardness at the interface between the HAZ and the thermomechanically affected zone (TMAZ). The hardness then increases slightly in the NG region of the welds. The hardness data also show that decreasing the

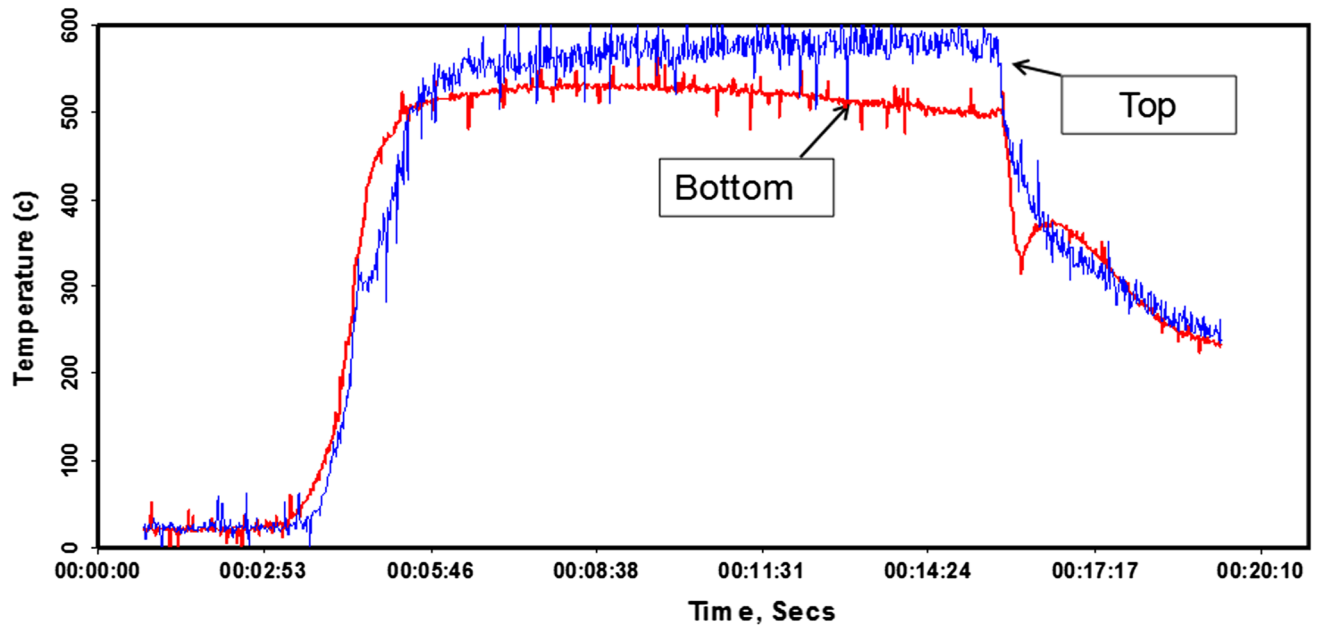


Fig. 5—An example of the measured temperature traces curves in the locations near the top and near the bottom of the tool for TPT1.

Table II. The Measured Temperatures, the Calculated Heat Input, and the Softened Region Width for the Welds

Item/Weld	TPT1	TPT2	PPT1	PPT2	PPT3
Torque (Nm)	225	260	300	329	200
Heat Input (KJ/mm)	4.523	13.1	6.03	16.536	6.03
Temperature at Top (°C)	560	592	622	634	—
Temperature at Base (°C)	530	546	577	570	—
HAZ Width (mm)	59.7	90	96	144	67.3

welding speed results in an increase of the HAZ width, which is a direct result of the increase of heat input.

The observed hardness profiles are typical for such alloys in which all the regions affected by the heat generated during FSW have a lower hardness than that of the base material. This decrease of hardness is believed to be either due to the dissolution or the coarsening of the precipitation hardening phase^[26–28] according to the thermal cycle experienced during FSW. Approximate locations of the different FSW zones is superimposed on the hardness maps with the boundaries of the NG regions in solid white lines, boundaries of the TMAZ in dashed white lines, and the boundaries of the HAZ in dashed black lines.

B. Temperature Measurement and Heat Input Calculations

Temperature was measured near the top surface and near the bottom of the NG using two thermocouples embedded within the tool. An example of the temperature trace curves of the TPT1 weld is shown in Figure 5, which shows that the temperature is higher near the top surface than that near the base of the NG.

Table II shows the measured peak temperatures, the calculated heat input, and the HAZ (softened region) width for all the welds. From this table it can be observed that the heat input and width of the softened region increases with decreasing welding speed.

C. Grain Structure

The grain structure near the top and near the bottom of the NG region of each weld at the vertical centerline was examined. For this purpose, high-resolution EBSD maps using a step size of 0.3 μm were acquired. EBSD maps are presented in Figures 6 and 7 as inverse pole figure (IPF) coloring with respect to the ND. Low-angle boundaries (LABs) of 5 to 15 deg (white lines) and high-angle boundaries (HAGBs) > 15 deg (black lines) are superimposed on the maps. For the TPT welds, Figure 6, it can be observed that the grain orientation is a mixture of $\langle 111 \rangle$ blue, $\langle 110 \rangle$ green, and $\langle 100 \rangle$ red. This mixture of grain orientation is due to the tilt of the data about the transverse direction (TD) axis due to the tapering of the tool. In terms of grain size, it can be clearly seen that the grain size is larger at the top (Figures 6(a) and (c)) of the NG than that near the

bottom of the NG (Figures 6(b) and (d)). This variation of grain size is mainly due to the variation in the total strain and the strain rate experienced from the top to the base, discussed in next section. The variation of strain rate and strain is expected to be due to the tapering of the tool used to produce the welds (TPT1 and TPT2). There is also a variation in the density of LABs from the top to the base of the NG with a higher density at the base of the NG.

The average grain size was calculated from the EBSD data for each map with only grains of misorientation > 15 deg and having more than four pixels considered, Table III. The grain size near the top of the NG is about double that near the base for TPT welds. Interestingly, no significant variation of the grain size can be observed by the decrease of the welding traverse speed from 125

to 62.5 mm/min for TPT1 and TPT2, respectively. On the other hand, a much more uniform grain size from the top to the bottom of the NG can be observed in the PPT welds, shown in Figures 7(a) through (f). This uniform grain structure must reflect the uniform strain and temperature experienced during FSW using the PPT. Again, no significant variation in the grain size can be observed by reducing the welding traverse speed from 125 to 62.5 mm/min for PPT1 and PPT2, respectively. Using a small diameter probe tool of 12 mm to produce PPT3 resulted in almost the same grain size relative to the large diameter probe tool of 19 mm that was used to produce the PPT1 weld at approximately the same processing conditions, expect for an increase in the rotation rate, which may be the cause of the slight increase in the grain size for PPT3.

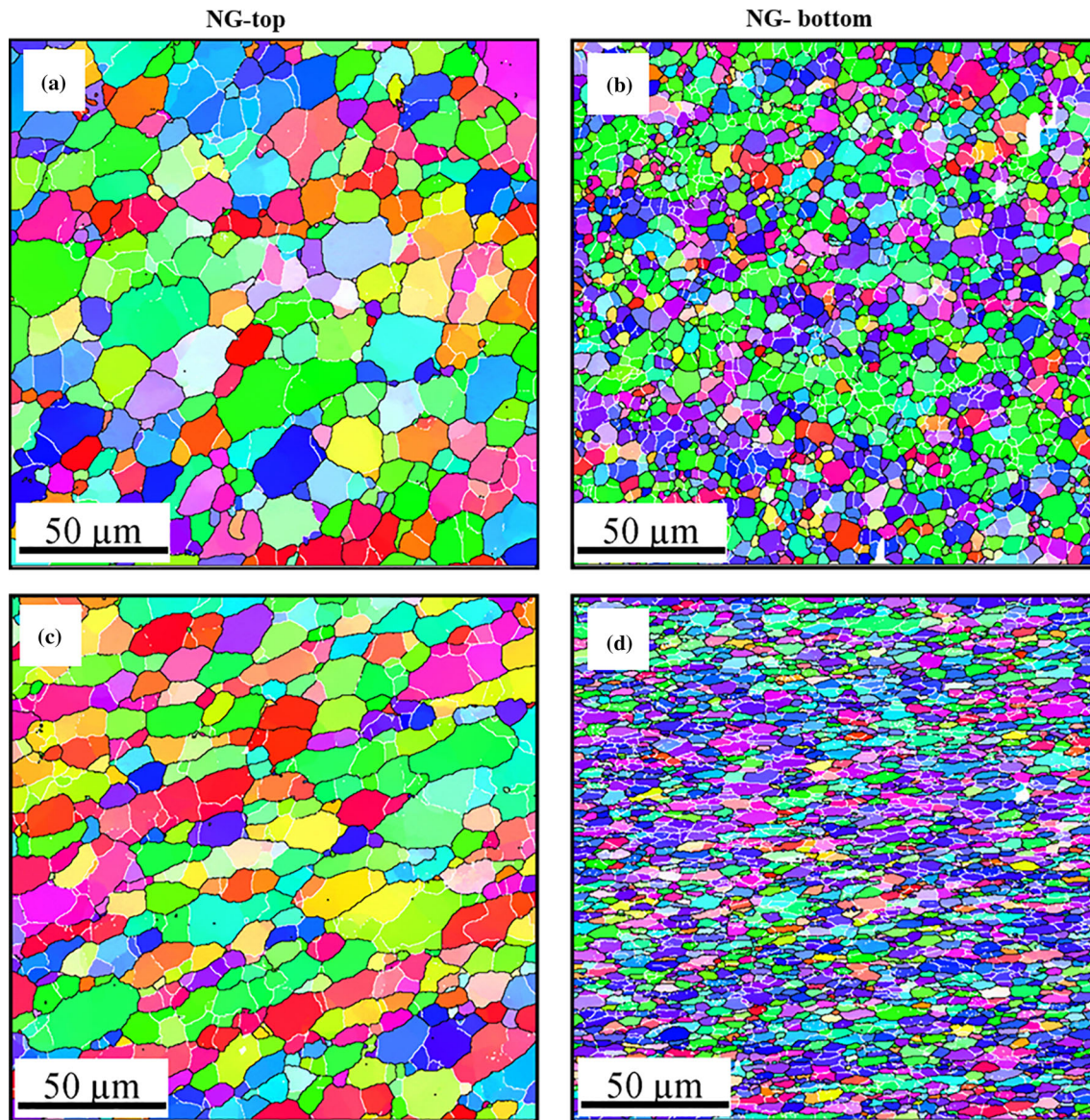


Fig. 6—EBSD maps at the NG in IPF coloring relative to the ND and the grain boundary maps superimposed, 2 to 15 deg in white lines and > 15 deg in black lines. (a, b) PPT1 and (c, d) PPT2 (Color figure online).

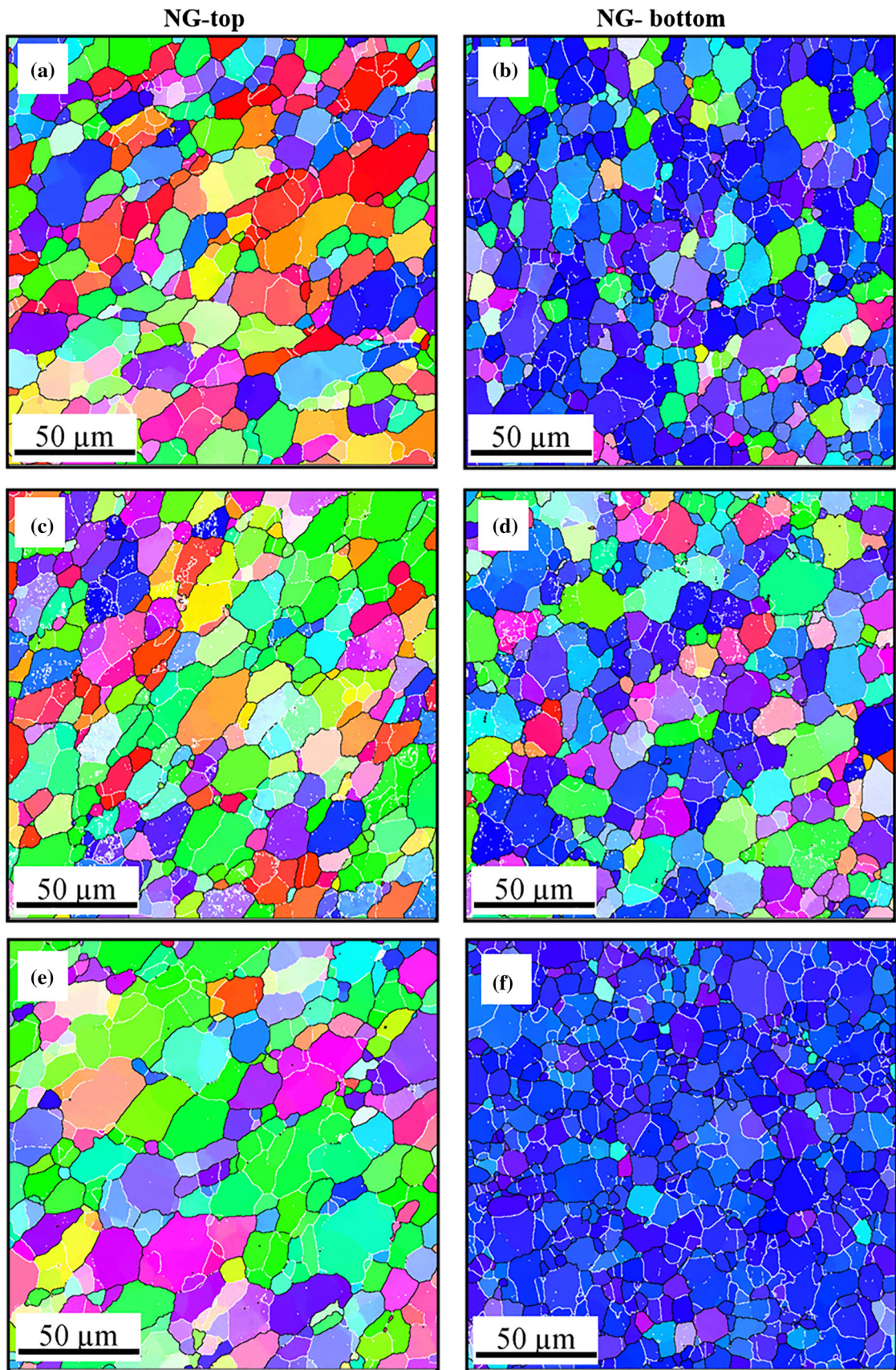


Fig. 7—EBSD maps at NG in IPF coloring relative to the ND and the grain boundary maps superimposed, 2 to 15 deg in white and > 15 deg in black. (a, b) PPT1, (c, d) PPT2, and (e, f) PPT3 (Color figure online).

D. Strain Rate and Zener–Hollomon Parameter Calculations

During FSW, the material experiences severe plastic deformation in the stirring zone; however, the strain rate experienced during this severe plastic deformation process has not yet been exactly determined. Many attempts have been made to calculate or estimate the strain rate during FSW.^[29–32] Chang *et al.*^[29] calculated the strain rate for friction stir weld of 6-mm-thick AZ31 Mg alloy. They suggested the strain rate varied from 5 to 50 s⁻¹ when the rotation rate was varied from 180 to 1800 rpm at constant travel speed of 90 mm/min. Gerlich *et al.*^[30] estimated the strain rate during friction stir spot welding of 7075-T6,^[30] AA5754, and AA6061.^[31] They reported that the strain rate decreased from 650 to 20 s⁻¹ when the rotation rate increased from 1000 to 3000 rpm in case of AA7075-T6 due to slippage during FSW, however, in the case of AA5754 and AA6061 they reported that the strain rate increased from 180 to 479 s⁻¹ and from 55 to 395 s⁻¹, respectively, when the rotation rate increased from 750 to 3000 rpm. More recently, Masaki *et al.*^[32] estimated the strain rate during FSW to be between 2 and 3 s⁻¹ by comparing FSW microstructures with plane strain compression test microstructures. This wide range of the strain rate from 2 to 650 s⁻¹ reported in the literature means that the strain rate during FSW/FSP is still not determined with a high degree of confidence.

In the current work, an approach is proposed to calculate the strain rate during FSW. Here we assume that the shear strain generated by the rotating probe is the dominant mechanism influencing plastic deformation, with the tool traverse motion having much less

influence. This is most likely the case in thick-section welds but is less likely to be true in thin-section welds. It should be noted that the NG dimensions are larger than the probe dimensions in terms of diameter and length, as can be seen from Figure 8, in which the exact tool shape is superimposed on the optical macrograph of the weld for the tapered tool weld and parallel tool weld, respectively. The difference between the NG radius (NG_r) and the probe tool radius (P_r) is assumed to be the thickness of the material sheared (S_x) around the tool probe at the rotation rate used in this work.

The shearing speed (V_s) can then be calculated using Eq. [1]

$$V_s = 2\omega P_r, \quad [1]$$

where $\omega = \frac{2\pi r}{60}$ and r is the rotation rate, rpm.

Although the practical contact condition in FSW reported to be partial sliding/sticking condition based on the FSW parameters,^[33] in the current calculation and for simplification, the sticking condition is considered. Accordingly, the shear strain rate ($\dot{\gamma}$) can be calculated according to Figure 9 using Eq. [2]:

$$\dot{\gamma} = \tan \alpha = \frac{V_s}{S_x}. \quad [2]$$

And the tensile strain rate can be calculated from Eq. [3]:

$$\dot{\epsilon} = \frac{\dot{\gamma}}{\sqrt{3}}, \quad [3]$$

Table III. EBSD Calculated Average Grain Size in the NG Region of the Welds

	TPT1	TPT2	PPT1	PPT2	PPT3
Grain Size at Top (μm)	11.20	11.86	14.816	14.48	16
Grain Size at Bottom (μm)	5.08	4.255	12.49	10.7	11.46

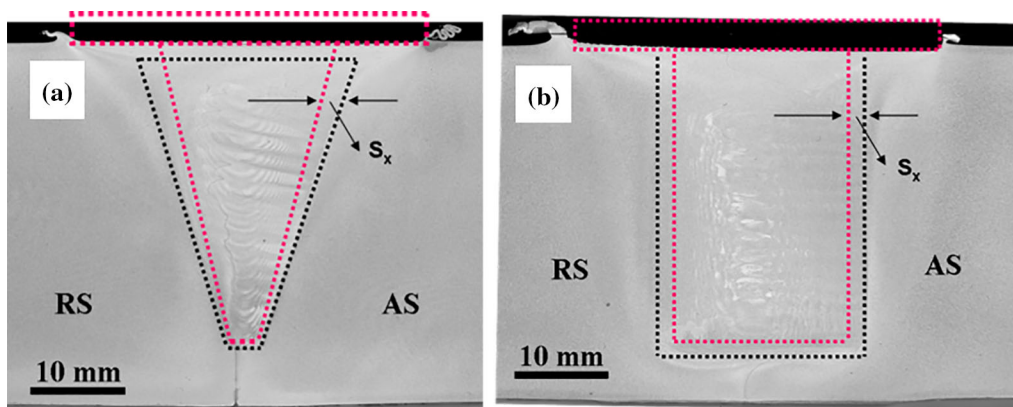


Fig. 8—A schematic of the tool shape superimposed on the optical macrograph of the weld showing how the thickness of the sheared material (S_x) can be measured for FSW. Red-dashed line represents the exact tool dimension and black-dashed line represents the NG. (a) Tapered probe tool and (b) parallel probe tool (Color figure online).

Using the proposed method, the equivalent tensile strain rates for the different welds were calculated near the top and near the base of each weld and are presented in Table IV.

It can be observed that the strain rate increases from the top to the bottom of the tapered tool welds. This is mainly due to the decrease in the thickness of the sheared material (S_x) from the top to the bottom of the weld as can be seen from Figure 8(a). The strain rate is constant from the top to the bottom of the parallel tool due to the constant thickness of sheared material from the top to the bottom. In both cases, the strain rate increased with the slight increase in the rotation rate.

Using the calculated strain rate $\dot{\epsilon}$, measured temperature T , activation energy Q of AA6082 (269 KJ/mol),^[34] and the gas constant R the values of the Zener–Hollomon parameter (the temperature-compensated strain rate) Z can be calculated using Eq. [4].

$$Z = \dot{\epsilon} \exp\left(\frac{Q}{RT}\right). \quad [4]$$

The relationship between the Zener–Hollomon parameter and the average grain size (d , μm) for AA6082 during FSW can then be established, as shown in Figure 10 and is given quantitatively by Eq. [5]

$$\ln d = 13.997 - 0.264 \ln Z. \quad [5]$$

E. Crystallographic Texture

For the crystallographic texture investigation, EBSD maps were acquired across the whole NG zones at the midsection of the welds (TPT1, TPT2, PPT1, and PPT2). Figure 8 shows the orientation image map (OIM) using IPF coloring with respect to the ND of the welds and the corresponding (111) pole figures at equal segments of the map, shown above each map. The OIM of weld TPT1 in Figure 11 clearly shows near

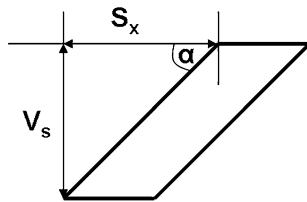


Fig. 9—Schematic of shear strain rate calculation.

vertical bands, which reduce in thickness from the center to the edge, of alternating near $\langle 110 \rangle$ (green) and near $\langle 111 \rangle$ (blue/purple) grain orientation across the whole NG as reported before.^[35,36]

In terms of texture, the whole NG for the weld is dominated by off-axis simple shear textures, as can be seen from the (111) PFs above the IPF maps in Figure 11. This off-axis simple shear texture has been reported to be the dominant texture in the NG region.^[34] The authors were able to show that the textures within the whole NG are equivalent and can be related to each other by two rotations: (1) a rotation (α) about the ND and (2) a constant tilt angle (β) about a direction perpendicular to ND.^[35] These two rotations were suggested to be mainly due to the rotation of the shear reference frame with the rotation of the tool and the tapering of the tool, respectively.^[35,36]

The EBSD data of TPT1 and TPT2 welds are presented before and after rotation correction in Figure 11; the raw data in (a), the rotated data in (b), and the texture components map in (c) of the TPT1 and TPT2 figures. It can be noted that increasing the heat input (TPT2) has resulted in a significant variation on the crystallographic with the disappearance of the banding structure that was observed at the low heat input weld (TPT1). It can be observed that the PFs before rotation show the off-axis simple shear texture that reduced in intensity towards the AS and after rotations, the simple shear texture can be seen with the B component more persistent than the B component towards the AS.

Figure 12 shows the OIM of the area analyzed in PPT1, PPT2, and PPT3 welds using IPF coloring with respect to the ND of the weld and the corresponding (111) pole figures of equal wide segments of the map are shown above the map for the raw data and below the map for the rotated data. The OIM of the PPT1 and

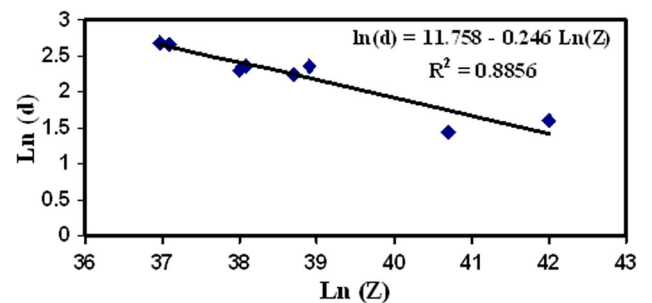


Fig. 10—Plot of the relationship between the grain size and Zener–Hollomon parameter for the FSWed AA6082.

Table IV. Calculated Strain Rate ($\dot{\epsilon}$) Data Near the Top and Near the Base of the Welds

Weld Name	TPT1	TPT2	PPT1	PPT2	PPT3
Strain Rate near Top (s^{-1})	166	209	282.6	353	217
Strain Rate near Base (s^{-1})	288	362	282.6	353	217
Z at the Top	2.9×10^{19}	8.5×10^{18}	3.2×10^{18}	2.4×10^{18}	—
Z at the Bottom	2.2×10^{20}	1.26×10^{20}	2.2×10^{19}	3.8×10^{19}	—

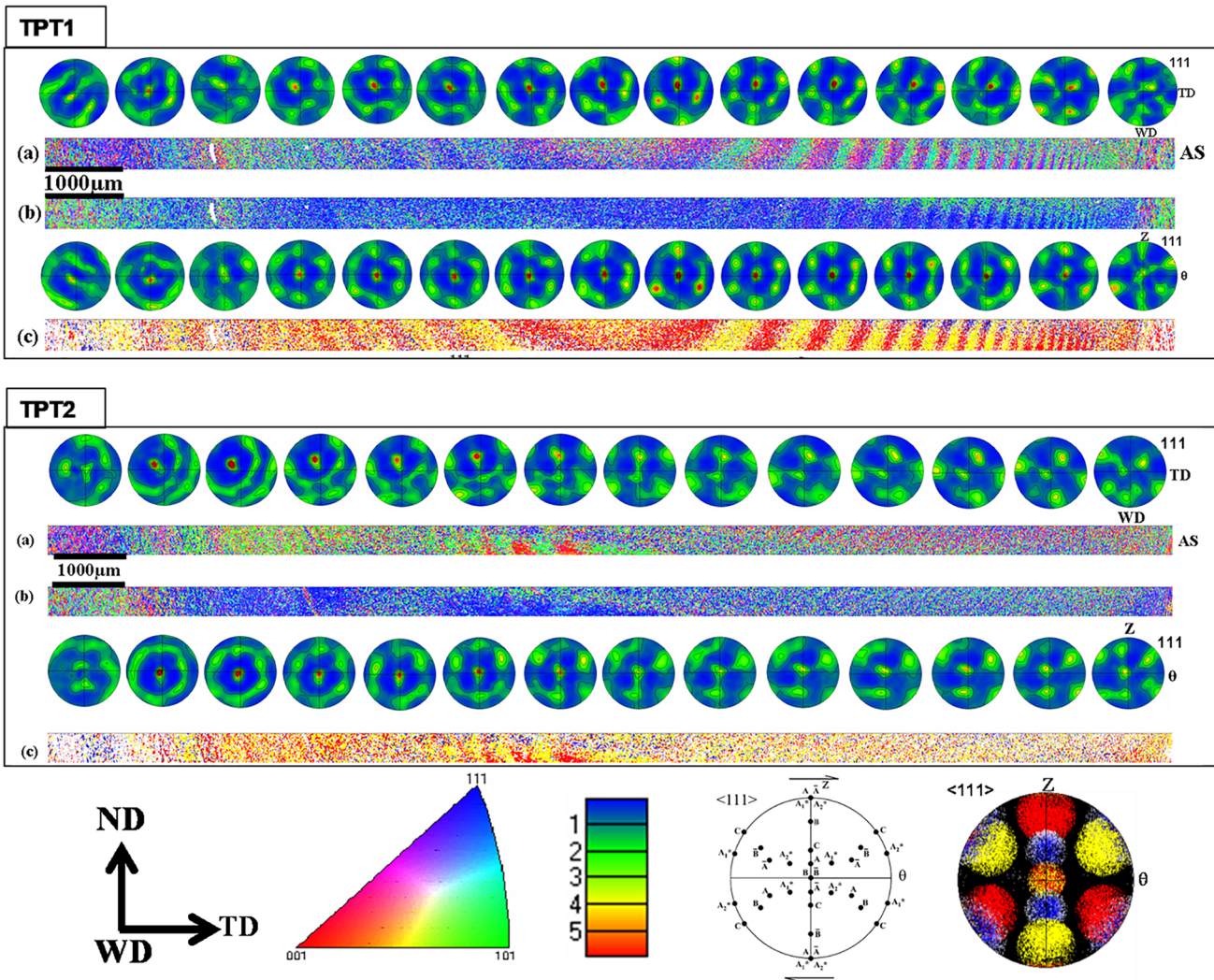


Fig. 11—(a) EBSD IPF coloring map with respect to ND across the whole NG of TPT1 and TPT2 welds and above the maps (111) pole figures in 15 equal wide segments. (b) EBSD map after rotation and the corresponding (111) pole figures. (c) Texture components map after rotation correction with B (red), \bar{B} (yellow), and C (blue). The IPF maps coloring key, PFs colorings key, and ideal simple shear texture positions in 111 PF (Color figure online).

PPT3 in Figure 12 clearly shows that the whole NG is completely dominated by $\langle 111 \rangle$ (blue) grain orientation with no obvious banding structure observed. It should be noted that the maps shown in this figure represent the data before and after rotation as there is no rotation about the ND for these maps because the welds were carried out using PPT.

In terms of texture before rotation the whole NG of PPT1 and PPT3 welds are dominated by the off-axis simple shear texture. The intense central (111) pole is in the center of the pole figures but there is still a systematic rotation of the texture components about the ND that can be seen clearly. At the extreme AS side of the NG, the intense central (111) pole of the shear texture lies in the WD plane parallel to the ND and this then rotates about the ND as a function of distance, x , from the center of the weld such that at the center, *i.e.*, $x = 0$, the (111) pole lies in the TD plane (still parallel

to the ND). At the extreme RS side, the (111) pole lies once again in the WD plane in the opposite direction to the AS and still parallel to the ND. This implies that the textures within the whole NG are equivalent and can be related to each other by only one rotation: a rotation (α) about the ND, which takes into account the rotation of the shear reference frame about ND with the rotation of the tool and this is shown schematically in Figure 13(a). The position of the local shear reference frame at every position behind the tool can be seen in Figure 13(b). It can be noted that the map of the weld produced at high heat input (PPT3) is slightly different in terms of grain orientation. This is especially true for the PFs towards the AS, which clearly shows mixed grain orientation and a weak texture of non-systematic rotation. This is similar to the high input weld produced with the TPT tool and explained above (TPT2). This can be attributed mainly to the high input that affects the flow of the

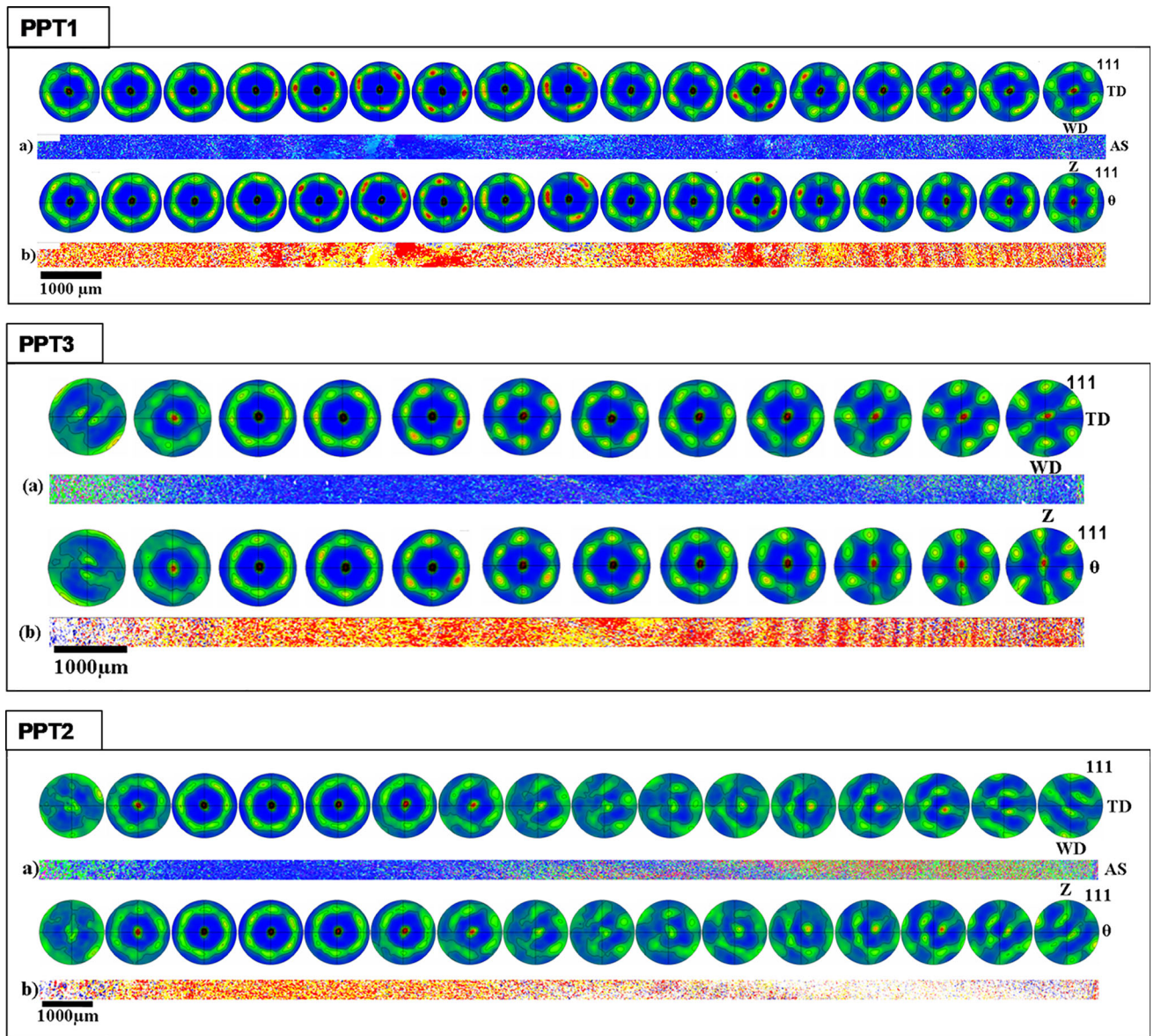


Fig. 12—(a) EBSD IPF coloring map with respect to ND across the whole NG of PPT1, PPT2, and PPT3 welds. Above the maps, the corresponding raw data (111) pole figures of equal wide segments and below the maps the corresponding rotated (111) PFs. (b) Texture components map after rotation correction with B (red), \bar{B} (yellow), and C (blue) (Color figure online).

material around the tool to the extent that gives the non-systematic behavior.

The rotated texture data are shown in Figure 12 (PPT1, PPT2, and PPT3) with the PFs below the maps. The PPT1 and PPT3 maps have similar behavior with all the NG dominated by simple shear texture. This is not applicable for the PPT2 map as mentioned above. Also from the texture component map shown below each dataset, which has highlighted the B (red), \bar{B} (yellow), and C (blue) components with a 25 deg spread, it can be seen that the B/ \bar{B} components are dominating the texture with some of C component at the AS and the RS edges. From the texture component map also it can be observed that the alternating bands between the (red) B/ \bar{B} (yellow)

clearly can be observed especially at the AS of the map.

A comparison between the overall texture across the whole NG for all the welds with respect to the local shear reference frame in terms of (011), (111) PFs and ODF sections at $\varphi = 0$ deg and $\varphi_2 = 45$ deg is illustrated in Figure 14. The crystallographic texture of the welds produced by the different tools (TPT and PPT) in the probe dominated region of the NG with respect to the local shear reference frame is dominated by simple shear texture with the B/ \bar{B} components dominating. The C component is observed only in the TPT welds as it can be seen from the ODF sections of these welds (TPT1 and TPT2). The main difference due to the tool geometry in terms of texture is that the TPT resulted in a tilt of the local

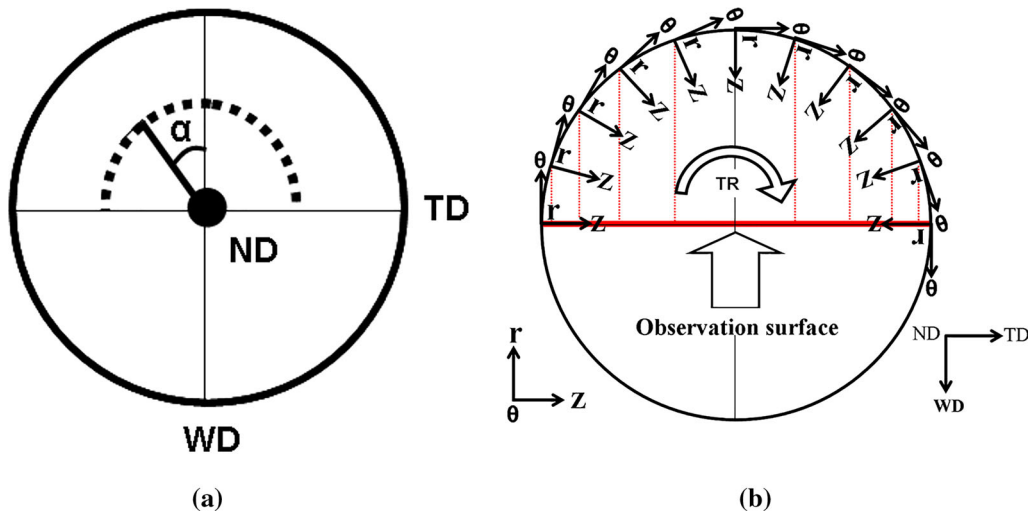


Fig. 13—(a) Schematic diagram of the location of the intense $\langle 111 \rangle$ pole of the shear texture at angles α . Note in the current analysis, α was considered positive for an anti-clockwise rotation about ND and negative for a clockwise rotation. (b) Schematic diagram showing the FSW local shear (θ , Z , r) reference frames.

shear reference frame by an angle β as a result of tapering of the probe. This tilt angle consequently resulted in the tilt of the $\langle 111 \rangle$ by the same angle from the ND, as shown schematically in Figure 15(a). However, in the case of the PPT, the $\langle 111 \rangle$ are parallel to the ND, as shown schematically in Figure 15(b). This variation on the orientation of the $\langle 111 \rangle$ between the TPT and PPT welds will have an effect on the mechanical properties of the welds, which will need more investigation.

IV. CONCLUSIONS

Detailed investigation of microstructure and crystallographic texture of thick-section FSWed aluminum alloy 6082 has been carried out and the following conclusions can be drawn:

1. Thick-section welded joints of 32 mm depth in a 38-mm-thick AA6082-T6 were successfully produced using a high depth-to-width tool ratio of above 0.8.
2. The use of a TPT resulted in a variation of the grain size in the NG through the joint thickness from $\sim 11 \mu\text{m}$ near the top surface to $5 \mu\text{m}$ near the base, with almost negligible effect for the welding speed. However, with the use of a PPT almost, the grain size is far more uniform.
3. The hardness of the base material of about 120 Hv has decreased in general in the weld zone with the

lowest hardness in the HAZ of about 60 Hv. The heat input greatly affected the width of the HAZ with a width of about 60 mm at the low heat input welds that increased up to about 144 mm in the high heat input welds.

4. An approach is proposed to calculate the strain rate during FSW of aluminum, and values between 217 and 362 s^{-1} were obtained. The strain rate varied from the top to the base of the NG in case of TPT welds and was almost uniform in the case of the PPT welds. This is the main tool geometry factor affecting microstructure evolution in the weld zone.
5. The main difference between the TPT and PPT geometries in terms of texture is that the TPT resulted in the tilt of the local shear reference frame by an angle, as a result of tapering of the probe. This tilt angle resulted in the tilt of the $\langle 111 \rangle$ pole of the shear texture by the same angle from the ND. However, in the case of the PPT, the $\langle 111 \rangle$ are parallel to the ND.
6. Increasing the heat input with the same tool geometry has affected the crystallographic texture in terms of texture intensity and the standard texture components across the whole NG.
7. The use of a smaller diameter parallel probe tool (12 mm) has resulted in a weld integrity similar to that produced with the large diameter tool (19 mm) of the same geometry.

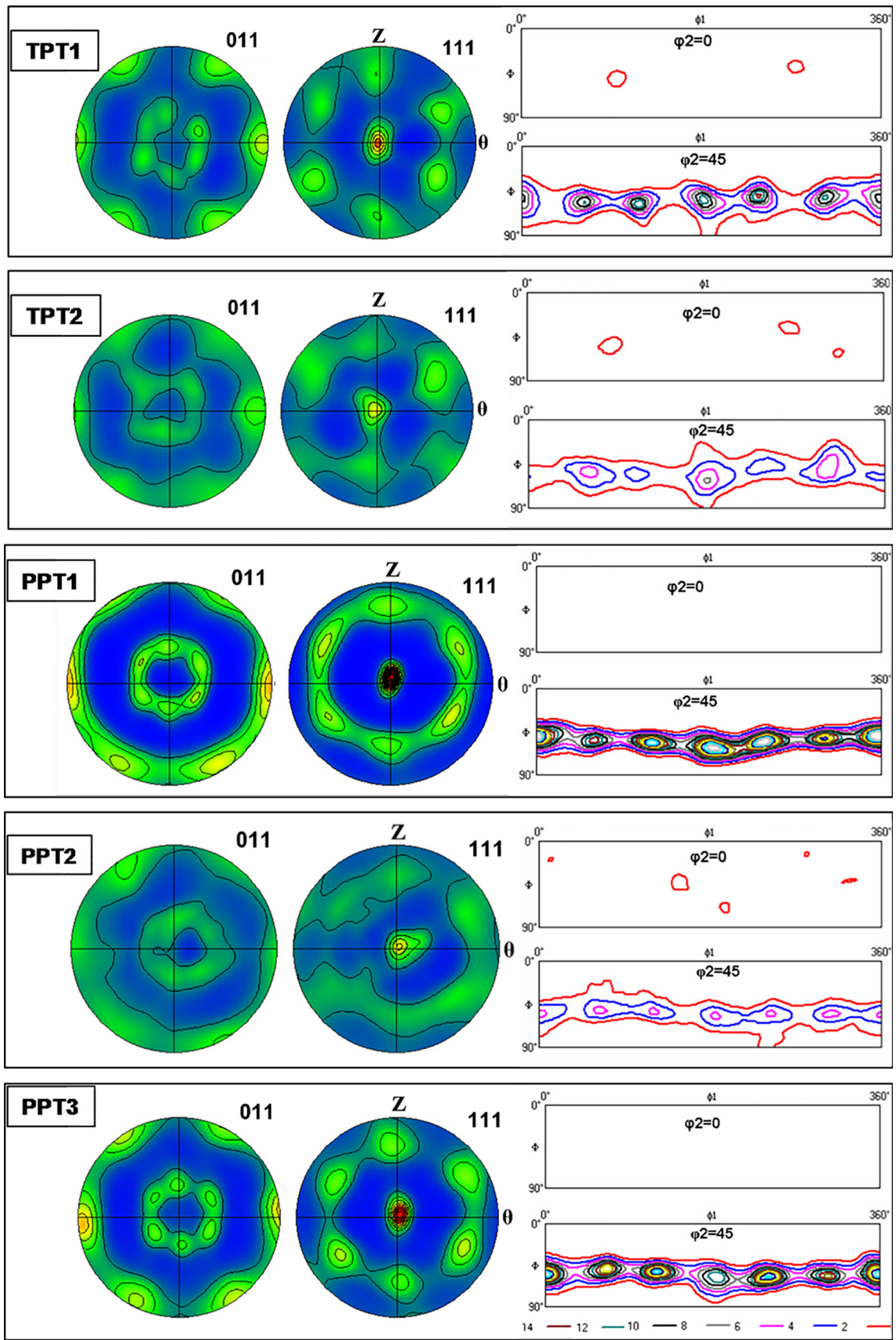


Fig. 14—(001), (111) PFs and ODF sections at $\phi = 0$ deg and $\phi = 45$ deg with respect to the local shear reference frame for the data collected across the whole NG from the different tool geometries and different heat inputs.

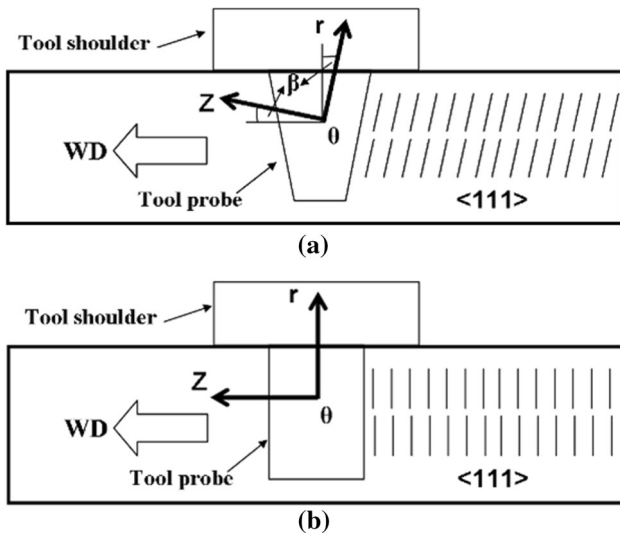


Fig. 15—Schematic view showing the trace of the $\langle 111 \rangle$ directions as well as the local shear reference frame (θ , Z , r) in case of (a) TPT welds and (b) PPT welds.

ACKNOWLEDGMENT

The author (MMZA) gratefully acknowledges the Egyptian Government for the financial support.

REFERENCES

1. W.M. Thomas, E.D. Nicholas, J.C. Needham, M.G. Murch, P. Templesmith, and C.J. Dawes, G.B. Patent Application No. 9125978.8, December 1991.
2. H. Hori and H. Hino: *Weld. Int.*, 2003, vol. 17 (4), pp. 287–92.
3. M. Enomoto: *Weld. Int.*, 2003, vol. 17 (5), pp. 341–45.
4. T. Kawasaki, T. Makino, K. Masai, H. Ohba, Y. Ina, and M. Ezumi: *JSME Int. J. Ser. A*, 2004, vol. 47 (3), pp. 502–11.
5. P.L. Threadgill, A.J. Leonard, H.R. Shercliff, and P.J. Withers: *Int. Mater. Rev.*, 2009, vol. 54 (2), pp. 49–93.
6. R. Rai, A. De, H.K.D.H. Bhadeshia, and T. DebRoy: *Sci. Technol. Weld. Join.*, 2011, vol. 16 (4), p. 325.
7. M.M.Z. Ahmed, E. Ahmed, A.S. Hamada, S.A. Khodir, M.M. El-Sayed Seleman, and B.P. Wynne: *Mater. Des.*, 2016, vol. 91, pp. 378–87.
8. M.M.Z. Ahmed, B.P. Wynne, and J.P. Martin: *Sci. Technol. Weld. Join.*, 2013, vol. 18 (8), p. 680.

9. M.M.Z. Ahmed, B.P. Wynne, W.M. Rainforth, and P.L. Threadgill: *Mater. Charact.*, 2012, vol. 64, pp. 107–17.
10. W. Woo, H. Choo, D. Brown, and Z. Feng: *Metall. Mater. Trans. A*, 2007, vol. 38A, pp. 69–76.
11. C. Sorensen and A. Stahl: *Metall. Mater. Trans. B*, 2007, vol. 38 (3), pp. 451–59.
12. A. Scialpi, L.A.C. De Filippis, and P. Cavaliere: *Mater. Des.*, 2007, vol. 28, pp. 1124–29.
13. A.L. Pilchak, M.C. Juhas, and J.C. Williams: *Metall. Mater. Trans. A*, 2007, vol. 38A, pp. 435–37.
14. J.G. Perrett, J. Martin, P.L. Threadgill, and M.M.Z. Ahmed: *Aluminium 2000 conference* 13–17 March, Florence, Italy, 2007.
15. K. Elangovan and V. Balasubramanian: *Mater. Sci. Eng. A*, 2007, vol. 459 (1–2), pp. 7–18.
16. H. Fujii, L. Cui, M. Maeda, and K. Nogi: *Mater. Sci. Eng. A*, 2006, vol. 419 (1–2), pp. 25–31.
17. M. Boz and A. Kurt: *Mater. Des.*, 2004, vol. 25 (4), pp. 343–47.
18. J. Zhang, P. Upadhyay, Y. Hovanski, and D.P. Field: *Metall. Mater. Trans. A*, 2004, vol. 49A, pp. 210–22.
19. J. Shen, F. Wang, U.F.H. Suhuddin, S. Hu, W. Li, and J.F. dos Santos: *Metall. Mater. Trans. A*, 2015, vol. 46A, pp. 2809–13.
20. J. Shen, S.B.M. Lage, U.F.H. Suhuddin, C. Bolfarini, and J.F. dos Santos: *Metall. Mater. Trans. A*, 2015, vol. 49A, pp. 241–54.
21. M. Imam, Y. Sun, H. Fujii, N. Ma, S. Tsutsumi, and H. Murakawa: *Metall. Mater. Trans. A*, 2017, vol. 48A, pp. 208–29.
22. H.R. Doude, J.A. Schneider, and A.C. Nunes: *Metall. Mater. Trans. A*, 2014, vol. 45A, pp. 4411–22.
23. M.-N.I. Avettand-Fenoel and R. Taillard: *Metall. Mater. Trans. A*, 2015, vol. 46A (1), pp. 300–14.
24. M.M.Z. Ahmed, S. Ataya, M.M. El-Sayed Seleman, H.R. Ammar, and E. Ahmed: *J. Mater. Process. Technol.*, 2017, vol. 242, pp. 77–91.
25. Y. Huang, Y. Xie, X. Meng, Z. Lv, and J. Cao: *J. Mater. Process. Technol.*, 2018, vol. 252, pp. 233–41.
26. J.Q. Su, T.W. Nelson, R. Mishra, and M. Mahoney: *Acta Mater.*, 2003, vol. 51 (3), pp. 713–29.
27. Y. Sato, M. Urata, and H. Kokawa: *Metall. Mater. Trans. A*, 2002, vol. 33A, pp. 625–35.
28. R. Fonda and J. Bingert: *Metall. Mater. Trans. A*, 2004, vol. 35A, pp. 1487–99.
29. C.I. Chang, C.J. Lee, and J.C. Huang: *Scripta Mater.*, 2004, vol. 51, pp. 509–14.
30. A. Gerlich, G. Avramovic-Cingara, and T. North: *Metall. Mater. Trans. A*, 2006, vol. 37A, pp. 2773–86.
31. A. Gerlich, M. Yamamoto, and T.H. North: *Metall. Mater. Trans. A*, 2007, vol. 38A, pp. 1291–1302.
32. K. Masaki, Y.S. Sato, M. Maeda, and H. Kokawa: *Scripta Mater.*, 2008, vol. 58 (5), pp. 355–60.
33. D.M. Neto and P. Neto: *Int. J. Adv. Manuf. Technol.*, 2013, vol. 65 (1–4), pp. 115–26.
34. M. Cabibbo, H.J. McQueen, E. Evangelista, S. Spigarelli, M. Di Paola, and A. Falchero: *Mater. Sci. Eng. A*, 2007, vols. 460–461, pp. 86–94.
35. M.M.Z. Ahmed, B.P. Wynne, W.M. Rainforth, and P.L. Threadgill: *Scripta Mater.*, 2008, vol. 59 (5), pp. 507–10.
36. M.M.Z. Ahmed, B.P. Wynne, M.M. El-Sayed Seleman, and W.M. Rainforth: *Mater. Des.*, 2016, vol. 103, pp. 259–67.